Severe Neurodegeneration with Impaired Autophagy Mechanism Triggered by Ostm1 Deficiency*

Céline Héraud[‡§], Adam Griffiths[‡§1], Subramanya N. M. Pandruvada[‡§], Manfred W. Kilimann[¶‖], Monica Pata[‡§], and Jean Vacher[‡§2]

From the [‡]Institut de Recherches Cliniques de Montréal (IRCM), Département de Médecine, Université de Montréal, Montréal, Québec H2W 1R7, Canada, the [§]Department of Medicine, Division of Experimental Medicine, McGill University, Montréal, Québec H3A 1A3, Canada, the [¶]Department of Otolaryngology, Göttingen University Medical Center, D-37075 Göttingen, Germany, and the [‖]Department of Molecular Neurobiology, Max-Planck-Institute for Experimental Medicine, D-37075 Göttingen, Germany

Background: Although loss of the *Ostm1* gene leads to the most severe form of osteopetrosis, *Ostm1* is expressed in other tissues, including the CNS.
Results: Independently of hematopoietic lineages, loss of Ostm1 results in acute neurodegeneration with enhanced autophagy.
Conclusion: We present evidence for an Ostm1 cell-autonomous role in neurons.
Significance: This study shows a novel molecular pathogenic mechanism for neurodegeneration-related diseases.

Loss of Ostm1 leads to the most severe form of osteopetrosis in mice and humans. Because functional rescue of the osteopetrotic defect in these mice extended their lifespan from ~3 weeks to 6 weeks, this unraveled a second essential role of Ostm1. We discovered that *Ostm1* is highly expressed in the mouse brain in neurons, microglia, and astrocytes. At 3–4 weeks of age, mice with Ostm1 loss showed 3–10-fold stimulation of reactive gliosis, with an increased astrocyte cell population and microglia activation. This inflammatory response was associated with marked retinal photoreceptor degeneration and massive neuronal loss in the brain. Intracellular characterization of neurons revealed abnormal storage of carbohydrates, lipids, and ubiquitinated proteins, combined with marked accumulation of autophagosomes that causes frequent axonal swelling. Stimulation of autophagy was provided by specific markers and by significant down-regulation of the mammalian target of rapamycin signaling, identifying a cellular pathologic mechanism. A series of transgenic mouse lines specifically targeted to distinct central nervous system cell subpopulations determined that Ostm1 has a primary and autonomous role in neuronal homeostasis. Complete functional complementation demonstrated that the development of severe and rapid neurodegeneration in these mice is independent of the hematopoietic lineage and has clinical implications for treatment of osteopetrosis. Importantly, this study establishes a novel neurodegenerative mouse model critical for understanding the multistep pathogenic cascade of cellular autophagy disorders toward therapeutic strategy design.

Among the different human bone diseases, one of the earliest and most debilitating disorders is osteopetrosis. Human osteopetrosis is a genetic disorder that results from hematopoietic cell defects affecting osteoclast lineage differentiation and/or maturation, responsible for bone resorption. Severe recessive forms of osteopetrosis in humans lead to rapid death, in contrast with mild dominant forms. Severe human osteopetrosis is frequently associated with several neuronal complications, anemia, and high susceptibility to infection (1). The neuronal complications have been secondarily ascribed to abnormal bone accumulation in osteopetrosis that compresses cranial nerves, resulting in optic atrophy and blindness as well as hearing impairment (2). However, there is recent evidence for primary central nervous system (CNS) defects in osteopetrotic patients with OSTM1 and ClC7 mutations (3–7). Of interest, OSTM1 mutations lead to both more severe osteopetrosis and CNS defects (8, 9).

The human *OSTM1* gene was identified subsequent to characterization of the genetic null mutation in the mouse *Ostm1* gene that is responsible for the severe osteopetrotic gl/gl phenotype. These gl/gl mice die within 3 weeks of age with defects in the osteoclast hematopoietic lineage (8, 10). The murine *Ostm1* gene is expressed in several tissues at variable levels. The Ostm1 expression pattern revealed high levels in hematopoietic lineages, including osteoclast, B-cells, and T-cells (11), as well as in the CNS, particularly the hippocampus and cerebellum (8). Ostm1 was shown to play essential roles in intracellular hematopoietic cross-talk from distinct transgenic mice targeting (11). *Ostm1* transgenic expression in hematopoietic lineages, in contrast to the osteoclast lineage, showed full hematopoietic and osteopetrotic complementation in gl/gl mice. Ostm1 was reported to interact with ClC7 (12, 13); however, ClC7 function in hematopoietic lineages is restricted to osteoclasts (14). Further, ClC7 systemic or conditional ablation is much less severe than in the gl/gl mice, consistent with human studies (15, 16). Besides the critical functions of Ostm1 demon-

strated in the hematopoietic lineages, the role of Ostm1 in the CNS independent of osteopetrosis has not been characterized.

To directly address the role of the *Ostm1* gene in extrahematopoietic tissues, we investigate the phenotype of the hematopoietic targeted *Ostm1* transgenic mice on the gl/gl background (PU.1-*Ostm1* gl/gl) (11) that have an extended lifespan but still undergo premature death. Cellular characterization of the CNS in transgenic PU.1-*Ostm1* gl/gl mice showed severe inflammatory responses by astrogliosis and microglia activation and showed major neuronal cell death associated with autophagosome accumulation, leading to rapid progression and widespread neurodegeneration. This study also establishes that Ostm1 has a neuronal cell-autonomous role, as determined from two series of specific CNS cell-targeted transgenic mouse lines with functional complementation in the hematopoietic rescued PU.1-*Ostm1* gl/gl mice. Therefore, Ostm1 is essential in hematopoietic lineages and, subsequently, solely in neurons for CNS homeostasis throughout the mouse lifespan.

EXPERIMENTAL PROCEDURES

Mice—The mouse strain GL/Le dl^J +/+ gl was obtained from the Jackson Laboratory (Bar Harbor, ME). Animal use complied with the guidelines of the Canadian Committee for Animal Protection and was approved by the local institutional animal care committee.

Production and Analysis of Transgenic Mice—The astrocyte-targeted specific construct (hGFAP-*Ostm1*) consisted of the human glial fibrillary acidic protein (hGFAP)[3] promotor (2.2 kb) linked to the *Ostm1* cDNA (1.055 kb) followed by an intron and a polyadenylation signal of the mouse protamine-1 gene (*mP-1*). The neuron-targeted specific construct (Syn1-*Ostm1*) was produced with the *Ostm1* cDNA linked to the 4.3-kb rat Syn1 promotor and the 240-bp SV40 poly(A) signal downstream. The hGFAP-*Ostm1* and Syn1-*Ostm1* fragments were excised from the plasmid vector, and transgenic mice were generated as described previously (11). Transgenic mice were identified by PCR with hGFAP forward (5′-CCGTGGTTGCTGTGTCTGTGTT-3′) and *mP-1* reverse (5′-TCTCACGTCAGGAGTTTGATGG-3′) primers and Syn1 forward (5′-ATTTAGTACCGCGGACAGAAGCCTT-3′) and HGH reverse (5′-AGTTGGGATGCCCTCACACTAGAA-3′). Each transgenic founder was successively crossed with heterozygous gl/+ mice to generate hGFAP-*Ostm1* gl/+ and Syn1-*Ostm1* gl/+ transgenic progenies. These progenies were then crossed with PU.1-*Ostm1* gl/+ mice to produce double transgenic PU.1-*Ostm1*-hGFAP-*Ostm1* gl/gl and PU.1-*Ostm1*-Syn1-*Ostm1* gl/gl mice, respectively.

Immunohistological Analysis—Anesthetized mice were perfused, and brains were postfixed overnight, followed by paraffin embedding. For cytoarchitectural studies, sections (4 μm) were stained by hematoxylin and eosin (H&E), periodic acid-Schiff, or Oil Red O on paraffin-embedded or frozen sections. For immunohistochemistry, sections were subjected to protease antigen retrieval (0.1% trypsin in 0.1% CaCl$_2$, 20 mM Tris-HCl,

pH 8.0) and peroxidase quenching and immunolabeled with the R.T.U. VECTASTAIN Universal ABC kit using the DAB substrate kit (Vector Laboratories) and counterstained with hematoxylin. For immunofluorescence, brain sections were exposed to trypsin, blocked for 1 h in 10% normal goat serum and 0.1% Triton X-100 in phosphate-buffered saline (PBS), and incubated overnight at 4 °C with the primary antibody and then with a goat anti-mouse Alexa-488 and a goat anti-rabbit Alexa 546 IgG (H + L) (Molecular Probes) for 1 h. The following primary antibodies were used: monoclonal mouse anti-NeuN (Chemicon), monoclonal mouse anti-calbindin-D-28K, monoclonal mouse anti-Gfap (Sigma), Isolectin Ib4 Alexa Fluor dye conjugates (Invitrogen), and rabbit polyclonal anti-IbaI (Wako) and rabbit polyclonal anti-ubiquitin (Dako). Apoptosis was analyzed by a TUNEL assay using the FragEL DNA fragmentation detection kit (Calbiochem) according to the manufacturer's recommendations. Sections were counterstained with methyl green and analyzed using Axiophot (Carl Zeiss) and Northern Eclipse acquisition software.

Ultrastructural Analyses—Anesthetized mice were perfused with PBS followed by fixative (1% paraformaldehyde and 2.5% glutaraldehyde), and brain tissue was postfixed for 2 h in the same fixative. Floating sections (50 μm) were postfixed in 1% OsO$_4$ in cacodylate buffer and dehydrated in ethanol series before embedding and polymerization in LR White Resin (Electron Microscopy Sciences). Hippocampal, cerebellar, and cortical brain ultrathin sections were stained on nickel grids with 1% uranyl acetate in 70% ethanol. For immunogold staining, ultrathin cortical brain sections were labeled with an anti-ubiquitin antibody, followed by incubation with an anti-rabbit antibody coupled to 18-nm gold beads (Jackson ImmunoResearch Laboratories) before staining with 1% uranyl acetate and lead citrate. Grids were viewed on a Jeol 1200-Ex transmission electron microscope (Jeol, Inc., Peabody, MA).

Neuronal and Astroglial Cell Quantification—Sagittal cerebral cortex sections ($n = 6$) immunostained with NeuN antibodies were used to quantify the neuronal population. Gfap-immunostained sections of hippocampus (three fields; magnification, ×40) and cortex (six fields; magnification, ×40) were used to evaluate astrocyte number and Gfap immunoreactivity using the Color Picker MatLab application (Mathworks) to determine the percentage of Gfap-stained pixel number per area. Data from at least three mice at 3 weeks of age and seven mice at 5 weeks of age were analyzed and submitted to statistical analysis. All images were captured via a live video camera (MicroPublisher version 3.3 RTV, QImaging) mounted onto an optic microscope (Axiophot, Carl Zeiss) or with a confocal microscope Axiovert 100M (Carl Zeiss). During this analysis, all parameters, including lamp intensity, video camera setup, and calibration, were maintained constant.

Primary Neuronal, Astrocyte, and Microglial Cell Cultures—Hippocampal neurons were prepared from P1 gl/gl and wild type littermates. Briefly, hippocampus was treated with papain (0.25% final) in Hanks' balanced salt solution for 20 min at 37 °C and mechanically triturated using fire-polished glass pipettes. Cells (~16 × 10^3 cells/cm^2) were plated on poly-L-lysine-coated glass coverslips and cultured in Dulbecco's modified

---

[3] The abbreviations used are: hGFAP, human glial fibrillary acidic protein; qPCR, quantitative real-time PCR; mTOR, mammalian target of rapamycin.

Eagle's medium (Invitrogen) supplemented with horse (5%) and fetal bovine serum (5%), glucose (6% v/v), penicillin (100 units/ml), and streptomycin (1 mg/ml) for the first 2 h and then changed to neurobasal medium containing antibiotics and B27 supplement (Invitrogen). Primary cultures of astrocytes were obtained from the cerebral cortex of neonate mice. Briefly, cerebral hemispheres were cleared off meninges, and then minced tissue was incubated in PBS containing 0.25% trypsin (Invitrogen) for 15 min at 37 °C. Dissociated cells ($\sim 50 \times 10^3$ cells/cm^2) were then resuspended in Dulbecco's modified Eagle's medium (Invitrogen) supplemented with horse (5%) and fetal bovine (5%) serum, glucose (5 mg/ml), penicillin (100 units/ml), and streptomycin (1 mg/ml). At confluence, free-floating microglia were collected following mild shaking (150 rpm for 2 h).

Expression Analyses—Gene expression in neurons and astrocytes was monitored using quantitative real-time PCR (qPCR). Total RNAs from neurons and astrocytes were isolated using TRIzol (Invitrogen) and reverse transcribed to obtain cDNA. Primers used in qPCR were as follows: *Ostm1* endogenous, forward (5′-GCTTCCTTCACTCAGAGCAA-3′) and reverse (5′-GTGAGAATGCAACTTGTCCGA-3′); hGFAP, forward (5′-GAGATTCGCACAATACGAGGCA-3′) and reverse (5′-GCGATAGTCGTTAGCTTCGTGCTT-3′); *NeuN*, forward (5′-TTGAGGTCAATAATGCCACAGCCC-3′) and reverse (5′-GAGGTGGTGCAGCTCGAAATGTAT-3′); *S16*, forward (5′-GCTACCAGGGCCTTTGAGATG-3′) and reverse (5′-AGGACGGATTTGCTGGTGTGG-3′). hGFAP-*Ostm1* and Syn1-*Ostm1* transgene expression was analyzed by qPCR with 0.1 μg of DNase (Invitrogen)-treated total RNA. Expression levels of the transgene were normalized with that of the endogenous gene expression (endogenous expression levels in nontransgenic were normalized to 1). The primers used for the hGFAP-*Ostm1* transgene were as follows: forward, 5′-GTGGTTGCTGTGTCTGTGTTCA-3′ (*Ostm1* exon 5); reverse, 5′-TCCTCCGTCTGCGACATCTTCG-3′ (hGFAP transgene). For the Syn1-*Ostm1* transgene, primers were as follows: forward, 5′-CGGCAGACAGAATGCAGATA-3′ (*Ostm1* exon 2); reverse, 5′-GCAGGTTATGCTCAAAGCAG-3′ (*Ostm1* exon 3). All reactions were performed in triplicate in a SYBR Green Master Mix (Qiagen). qPCR conditions were as follows: 94 °C for 15 min, followed by 40 cycles of 94 °C for 0.5 min, 60 °C for 0.5 min, and 72 °C for 0.5 min in an MX4000 Mutiplex quantitative PCR analyzer. PU.1-*Ostm1* transgene expression in microglia was assayed by semiquantitative RT-PCR using 0.5 mg of total RNA. The primers used were as follows: *Ostm1* endogenous, forward (5′-GCTTCCTTCACTCAGAGCAA-3′) (*Ostm1* exon 5) and reverse (5′-GTGAGAATGCAACTTGTCCGA-3′) (*Ostm1* exon 6); PU.1-*Ostm1* transgene, forward (5′-GCTTCCTTCACTCAGAGCAA-3′) (*Ostm1* exon 5) and reverse (5′-AGTGAATAGGAACTTCGGAA-3′) (EGFP). PCR conditions were as follows: 94 °C for 5 min, followed by 40 cycles of 94 °C for 0.5 min, 60 °C for 0.5 min, and 72 °C for 0.5 min.

Protein extracts were prepared from mouse brain homogenized in ice-cold radioimmune precipitation buffer and analyzed by Western blotting. Blots were probed with either mouse monoclonal anti-Gfap, polyclonal rabbit anti-LC3 (Sigma),

polyclonal rabbit Beclin-1 (Santa Cruz Biotechnology), polyclonal rabbit Akt, polyclonal rabbit phospho-Akt (Ser-473), anti-phospho-p70S6 kinase (Thr-390), anti-p70S6 kinase, anti-phospho-mTOR (Ser-2421), anti-mTOR (Cell Signaling), anti-β-actin (BD Biosciences), peroxidase-conjugated goat anti-mouse IgG (H + L), and/or a goat anti-rabbit IgG (H + L) (Bio-Rad). Signals were revealed by the ECL detection system (Amersham Biosciences) and quantified by densitometry using ImageQuant (GE Healthcare). Values were normalized relative to β-actin as controls.

Magnetic Resonance Imaging (MRI)—For MRI structural imaging, each mouse was anesthetized with isoflurane 1–2%, placed in the supine position onto the scanner bed, covered with a warm water-circulating blanket, and loaded into the 7T Bruker Pharmascan MRI scanner. IR-3D Turbo RARE images were acquired for deformation-based morphometric analysis with a total scan time of 50 min. During the entire procedure, animals were under continual anesthesia inhalation and monitored for respiration, cardiac rate, and rectal temperature (SA Instruments Inc.). At the end of image acquisition, each mouse was monitored for full recovery from anesthesia.

Statistical Analysis—Values are expressed as mean ± S.E. Unpaired two-sample Student's *t* test was used for statistical analysis, with $p < 0.05$ considered significant.

RESULTS

Extrahematopoietic Role of Ostm1—To examine the role of Ostm1 in the CNS, the gray-lethal gl/gl mice that develop hematopoietic and osteopetrotic defects were backcrossed to our transgenic mice expressing Ostm1 specifically in the early hematopoietic lineages with PU.1 regulatory sequences. The PU.1-*Ostm1* bacterial artificial chromosome transgenic mice on the gl/gl background display full correction of the hematopoietic defects (11). Compared with the spontaneous gl/gl mice (8), the mean lifespan of PU.1-*Ostm1* gl/gl mice was extended from 3 weeks to 5.4 weeks (Fig. 1*A*). This premature death of the PU.1-*Ostm1* gl/gl mice revealed an additional role for the Ostm1 gene independent of hematopoiesis.

Because Ostm1 expression is normally highly expressed in wild-type brain but is undetectable in brain from gl/gl homozygous mice (Fig. 1*B*), we investigated whether Ostm1 plays an essential role in the CNS. *Ostm1* subcellular expression was analyzed in microglia, neurons, and astrocytes in wild type and in PU.1-*Ostm1* gl/gl mice. Because weak *Ostm1* expression was detected in total brain of PU.1-*Ostm1* gl/gl in comparison with gl/gl mice (11), we questioned whether the microglia, considered to be brain macrophages that derive from hematopoietic lineages (17), are targeted with the PU.1 regulatory elements. Indeed, using qPCR, we found that the PU.1-*Ostm1* transgene was highly expressed in enriched microglial cells compared with wild-type controls, whereas the PU.1 endogenous expression was readily detectable and unaltered (data not shown). Neurons, astrocytes, and microglia, three predominant CNS cell populations, were isolated and enriched *ex vivo* by cell culture from wild type and gl/gl mice for expression analyses using qPCR. To validate the cell enrichment efficiency, expression of specific neuronal and astrocyte markers was monitored using neuronal nuclei (NeuN), glial fibrillary acidic protein (Gfap),
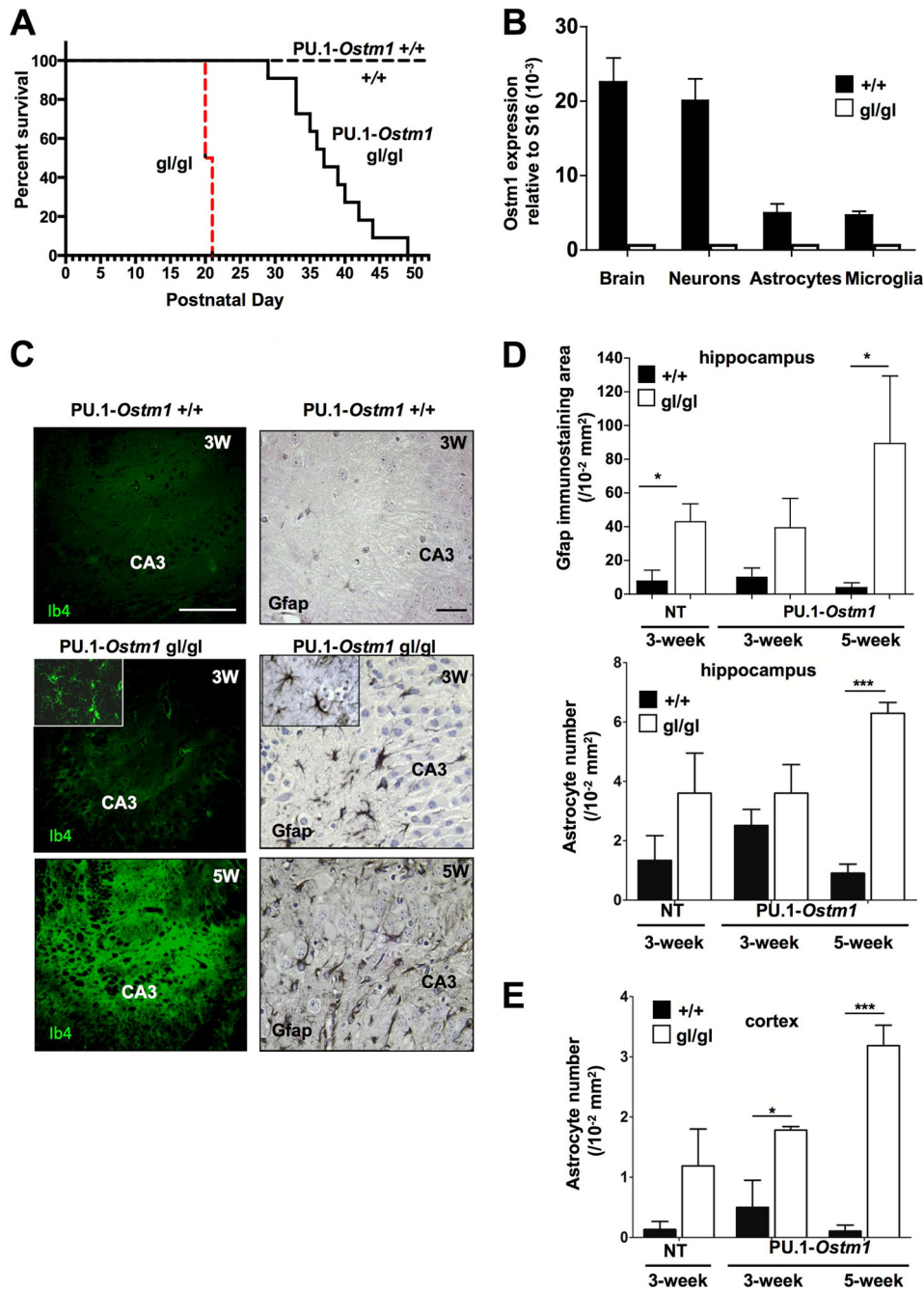
FIGURE 1. **Premature death and inflammatory response in PU.1-*Ostm1* gl/gl mice.** *A*, Kaplan-Meier curve of PU.1-*Ostm1* gl/gl mice ($n = 15$) compared with controls PU.1-*Ostm1* +/+ ($n = 8$), wild type +/+ ($n = 8$), and gl/gl ($n = 10$) mice. The PU.1-*Ostm1* gl/gl mice displayed a significant longer lifespan than the gl/gl mice but abrogated. *B*, histogram of Ostm1 expression analysis by qPCR from total brain and from enriched neuronal, astrocyte, and microglial cell populations of wild type and gl/gl mice. Ostm1 is expressed at high levels in neurons and moderately in astrocytes and microglia but is undetectable in gl/gl tissues or cells. *C*, analysis of the hippocampus CA3 layer from 3- and 5-week-old (*3W* and *5W*) PU.1-*Ostm1* gl/gl mice was performed with the microglial activation marker Ib4 (*left panels*; *scale bar*, 100 μm) and structural marker Gfap (*right panels*; *scale bar*, 50 μm) immunostaining. Compared with 3-week PU.1-*Ostm1* +/+ control mice, important microgliosis and astrogliosis were detected. *D*, quantification of astrocyte Gfap immunostaining area and cell population in hippocampus was carried out in non-transgenic (*NT*) wild type (+/+, *black bars*; $n = 3$) and mutated (gl/gl, *open bars*; $n = 3$) Ostm1 endogenous locus and in transgenic PU.1-*Ostm1* with wild type (+/+, *black bars*; $n = 3$) or null (gl/gl, *open bars*; $n = 3$) endogenous Ostm1 gene, at 3 weeks of age. In addition, 5-week-old transgenic PU.1-*Ostm1* with wild type (+/+, *black bars*; $n = 7$) or null (gl/gl, *open bars*; $n = 7$) Ostm1 gene were analyzed. *, $p < 0.05$; ***, $p < 0.001$. *E*, quantification of astrocyte cell population in cerebral cortex was performed in 3-week-old non-transgenic wild type (+/+, *black bars*; $n = 3$) and null (gl/gl, *open bars*; $n = 3$) Ostm1 endogenous locus and in 3- and 5-week-old transgenic PU.1-*Ostm1* with wild type (+/+, *black bars*; $n = 3$ and 7) and null (gl/gl, *open bars*; $n = 3$ and 7) endogenous Ostm1 gene. *, $p < 0.05$; ***, $p < 0.001$. *Error bars*, S.E.

and isolectin Ib4, respectively (data not shown). As shown in Fig. 1*B*, *Ostm1* expression was high in neuronal cells, whereas it was lower in astrocytes and microglia relative to the internal ribosomal S16 control. Therefore, the absence of Ostm1

expression associated with early death of PU.1-*Ostm1* gl/gl mice suggested that both cell populations, neurons and astrocytes, could be implicated in the phenotype and were thus characterized further.

Ostm1 and Neuronal Homeostasis

CNS Inflammatory Response in PU.1-Ostm1 gl/gl Mice—To analyze the role of Ostm1 in the brain, the populations of astrocytes and microglia in the mouse brains of PU.1-*Ostm1* gl/gl were compared with PU.1-*Ostm1* +/+ transgenic and/or wild type controls. Because one of the primary and frequent events occurring in abnormal brain phenotypes is an inflammatory response, we assessed the microglia and astrocyte population in these mice beginning at 2 weeks of age because no phenotype was detectable at 1 week. To determine the impact of the gl mutation on microglia, microglial cell activation was monitored using specific Ib4 isolectin immunostaining on brain sections from mice 3 and 5 weeks old. Interestingly, a significant and progressive increase in reactive microglial cell numbers was observed in the hippocampus and cerebral cortex of PU.1-*Ostm1* gl/gl mice compared with PU.1-*Ostm1* +/+ mice (Fig. 1*C*). In addition to this activation, microglial cells in the hippocampus of PU.1-*Ostm1* gl/gl mice displayed positive staining with the Iba1-Ca^{2+}-binding protein at 5 weeks of age, indicating an active phagocytic state. This microglial physiologic response occurs despite *Ostm1* expression, suggesting an effect from either inappropriate *Ostm1* levels or a secondary response mechanism. In parallel, widespread astrogliosis was detected in the hippocampus and cerebral cortex from PU.1-*Ostm1* gl/gl brain sections, as shown by Gfap immunostaining (Fig. 1*C*). Astrocyte Gfap immunostaining area in hippocampus was ~3- and ~12-fold higher at 3 and 5 weeks, respectively, when compared with controls (Fig. 1*D*). The astrocyte cell populations from the hippocampus and cerebral cortex were quantified in PU.1-*Ostm1* gl/gl and PU.1-*Ostm1* +/+ at 3 and 5 weeks, as well as in gl/gl mice at 3 weeks of age. The number of astrocytes in the hippocampus of 3-week-old gl/gl and PU.1-*Ostm1* gl/gl was not significantly different from controls, and at 5 weeks, the cell population had increased by ~7-fold (Fig. 1*D*). This indicates that the gl/gl mutation in astrocytes leads to an increase in cell population and more intense immunoreactive signal, in part due to cellular expansion. In the cerebral cortex, the astrocyte cell population was also increased relative to controls by ~9-fold for gl/gl and ~4-fold for PU.1-*Ostm1* gl/gl at 3 weeks of age and ~30-fold at 5 weeks of age in PU.1-*Ostm1* gl/gl mice (Fig. 1*E*). The enlarged cellular astrocyte population in the cerebral cortex occurred with a more rapid temporal response than in the hippocampus. Thus, PU.1-*Ostm1* gl/gl mice exhibit a rapid onset and progressive development of CNS gliosis, an inflammatory response that could be directly responsible for the phenotype or may result indirectly from neuronal damage.

Severe and Massive Neurodegeneration in PU.1-Ostm1 gl/gl Transgenic Mice—To decipher whether high Ostm1 expression in neurons has a direct role and indirectly induces a severe inflammatory status, the CNS cytoarchitectural structure was analyzed upon loss of Ostm1 expression in PU.1-*Ostm1* gl/gl transgenic mice. Immunostaining of brain sections for the neuron-specific NeuN protein showed mild cell loss in the hippocampus of PU.1-*Ostm1* gl/gl mice by 2–3 weeks of age and massive neurodegeneration by 5 weeks of age (*5W*) (Fig. 2*A*), whereas gl/gl mice do not display any defect by 2 weeks of age. This defect was widespread, particularly affecting cells of the CA3 and CA2 layers and the structure of the CA1 and GCL cell layers. Similarly, neuronal loss was also detected in four cell layers of the cerebral cortex in PU.1-*Ostm1* gl/gl relative to PU.1-*Ostm1* +/+ control mice (Fig. 2*B*). Quantification of the cortical neuronal population at 5 weeks of age revealed a substantial 30% reduction in PU.1-*Ostm1* gl/gl mice (Fig. 2*B*). In addition, a major deficit of Purkinje cells in the cerebellum, undetectable at 5 weeks, was readily apparent in 6-week-old (*6W*) PU.1-*Ostm1* gl/gl mice (Fig. 2*C*), and the cells had virtually disappeared by 7 weeks of age. Analyses of 6-week-old PU.1-*Ostm1* gl/gl transgenic mice using MRI showed severe neurodegeneration with thinning of the corpus callosum and enlargement of the lateral ventricles, confirming the reduced cortex thickness and hippocampus degeneration detected by histologic analyses. To determine whether the cell loss occurred via an apoptotic cell death mechanism, TUNEL assays were performed on sections from PU.1-*Ostm1* gl/gl and PU.1-*Ostm1* +/+ control mice at 3–5 weeks of age (data not shown). Interestingly, very few cells displayed TUNEL positivity, indicating that degenerating neurons are not eliminated through apoptosis, as shown for some human neurodegenerative diseases (18).

To determine whether neuronal loss was a general phenomenon, we investigated the retina of PU.1-*Ostm1* gl/gl mice. At 3 weeks of age (*3W*), the gl/gl and the transgenic PU.1-*Ostm1* gl/gl mice displayed considerable retinal degeneration with marked loss of photoreceptors, bipolar, amacrine, and horizontal cells (Fig. 2*D*). In fact, neuronal cell loss in the retina is the first evidence of pronounced cellular degeneration in PU.1-*Ostm1* gl/gl mice. Degeneration of all photoreceptor layers causes major retinal atrophy with advancing age in PU.1-*Ostm1* gl/gl mice (Fig. 2*D*). Thus, Ostm1 ablation leads to severe neuronal loss, starting about 3 weeks after birth, that progresses with age and affects all parts of the CNS, indicative of a potential intrinsic role for Ostm1 in neurons and excluding an early developmental defect.

Ostm1 Modulates Neuronal Metabolism—The wide spectrum of neuronal cell loss in different regions of the CNS prompted us to analyze the molecular mechanism responsible for neuronal cell loss. To further define the potential pathological mechanism of PU.1-*Ostm1* gl/gl in the CNS, cellular analyses of neurons and astrocytes were performed. Based on different degenerative brain pathologies, such as Parkinson and Huntington disease (19), that display cytosolic accumulation of ubiquitin-positive proteins, we monitored the protein-processing mechanism by assessing free and/or conjugated ubiquitin levels. Cortical sections of PU.1-*Ostm1* gl/gl and PU.1-*Ostm1* +/+ mice were co-immunostained for Gfap and ubiquitin from 3 weeks onward. As shown in Fig. 3*A*, astrocytes identified by Gfap-positive staining in PU.1-*Ostm1* gl/gl sections from 4-week-old mice did not display significant ubiquitin accumulation, suggesting no apparent cellular metabolic defect. In contrast, neurons from brain sections of 3- or 4-week-old PU.1-*Ostm1* gl/gl mice co-immunostained with NeuN/ubiquitin and displayed strong cytosolic ubiquitin accumulation compared with controls (Fig. 3*A*). Abundant ubiquitin accumulation in neurons from the hippocampus and cerebral cortex correlated with major cell degeneration. These analyses provide evidence that loss of Ostm1 results in abnormal protein turnover in neurons.
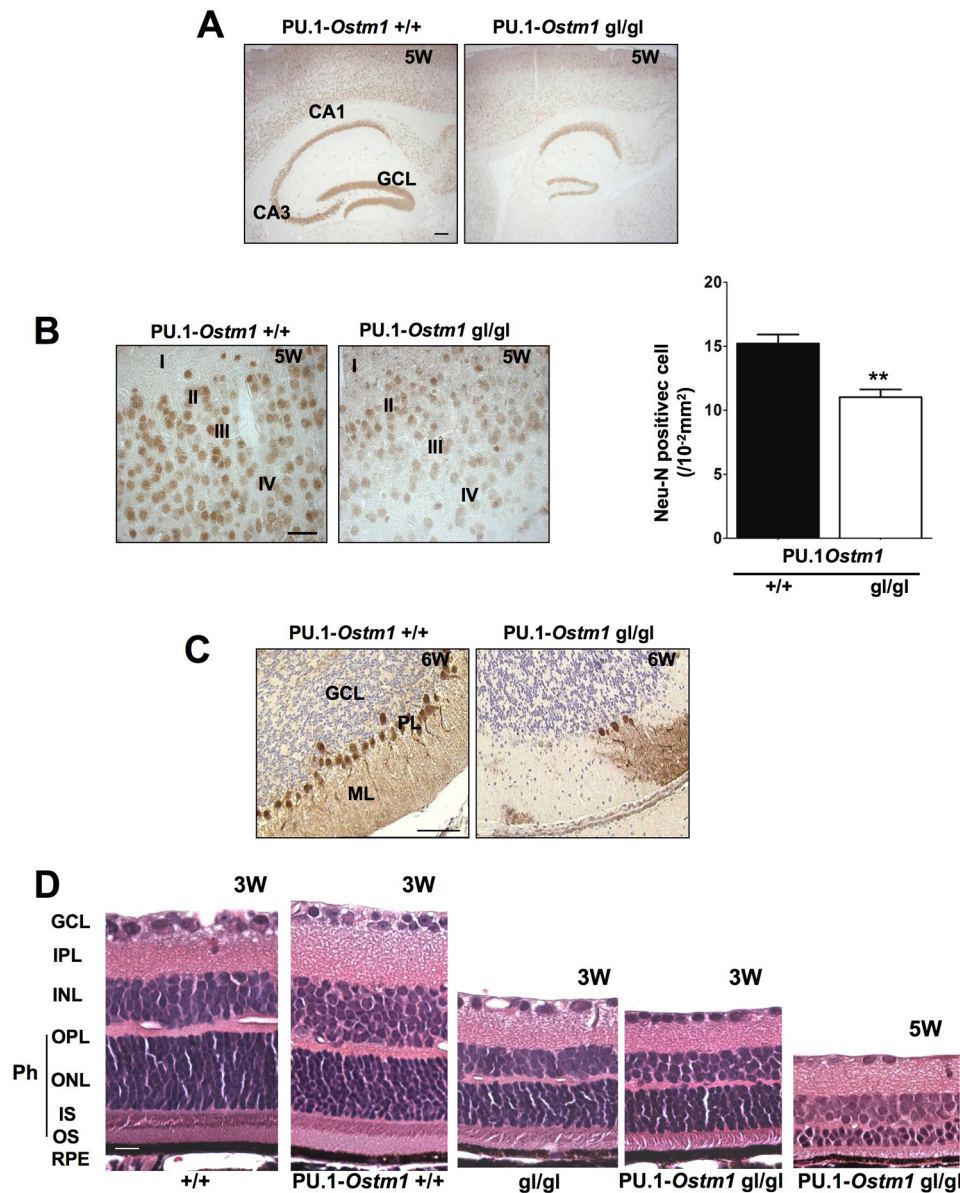
FIGURE 2. **Severe neurodegeneration in PU.1-*Ostm1* gl/gl mice.** *A,* loss of the CA3 layer of the hippocampus and granular cells of dentate gyrus was readily noticed in 5-week-old (*5W*) PU.1-*Ostm1* gl/gl mice compared with controls by NeuN immunostaining. *CA1* and *CA3,* pyramidal cell layers; *GCL,* granular cell layer. *Scale bar,* 100 μm. *B,* cerebral cortex sections of 5-week-old PU.1-*Ostm1* gl/gl mice immunostained with NeuN display a significant decrease in cortical neuron number compared with controls. *I–IV,* cortical neuronal cell layers. **, $p < 0.01$. *Scale bar,* 50 μm. *C,* cerebellum sections of 6-week-old (*6W*) PU.1-*Ostm1* gl/gl mice immunostained with Calbindin exhibit a massive loss of Purkinje cells relative to controls. *ML,* molecular layer; *PL,* Purkinje cell layer. *Scale bar,* 20 μm. *D,* PU.1-*Ostm1* gl/gl retina at 3 and 5 weeks old displayed important loss of photoreceptors (*Ph*) in comparison with control wild type (+/+) and PU1-*Ostm1* +/+ retina, whereas it was similar to 3-week-old gl/gl mouse retina. *IPL,* inner plexiform layer; *INL,* inner nuclear layer (bipolar, horizontal, and amacrine cells); *OPL,* outer plexiform layer; *ONL,* outer nuclear layer; *IS,* inner segment; *OS,* outer segment; *RPE,* retinal pigmented epithelium (H&E staining). *Scale bar,* 1 mm. *Error bars,* S.E.

In an attempt to define the type of neurodegenerative disease caused by Ostm1 among the various subgroups, we questioned whether cellular carbohydrate and lipid metabolism could be altered in addition to the abnormal protein accumulation observed in PU.1-*Ostm1* gl/gl. To examine glycogen metabolism in the transgenic PU.1-*Ostm1* gl/gl and gl/gl neurons, brain sections from 2–7-week-old mice were stained with periodic acid-Schiff to identify glycol conjugates. At 3 weeks of age (*3W*), these mice displayed enhanced intracellular storage of glycogen, glycolipids, and/or glycoproteins in pyramidal cells compared with controls (Fig. 3*B*). Extensive glycogen accumulation was also noted in all layers of the cerebral cortex and

hippocampus, particularly in the CA3 layer, suggesting a general and important deregulation of cellular carbohydrate storage. Furthermore, lipid metabolism was also analyzed in PU.1-*Ostm1* gl/gl brain sections at 3 weeks of age and onward using Oil Red O, which stains neutral lipids. Both the cerebral cortex and hippocampus showed important neuronal intracellular lipid accumulation by 5 weeks of age in PU.1-*Ostm1* gl/gl mice relative to control (Fig. 3*C*), suggesting also altered lipoprotein accumulation. In addition, extracellular lipid droplet build-up was also present in the CA3 layer of the hippocampus overlying the region where numerous pyramidal neurons are lost (Fig. 3*D*). Together, enhanced neuronal cytoplasmic storage of ubiquitin, carbohy-
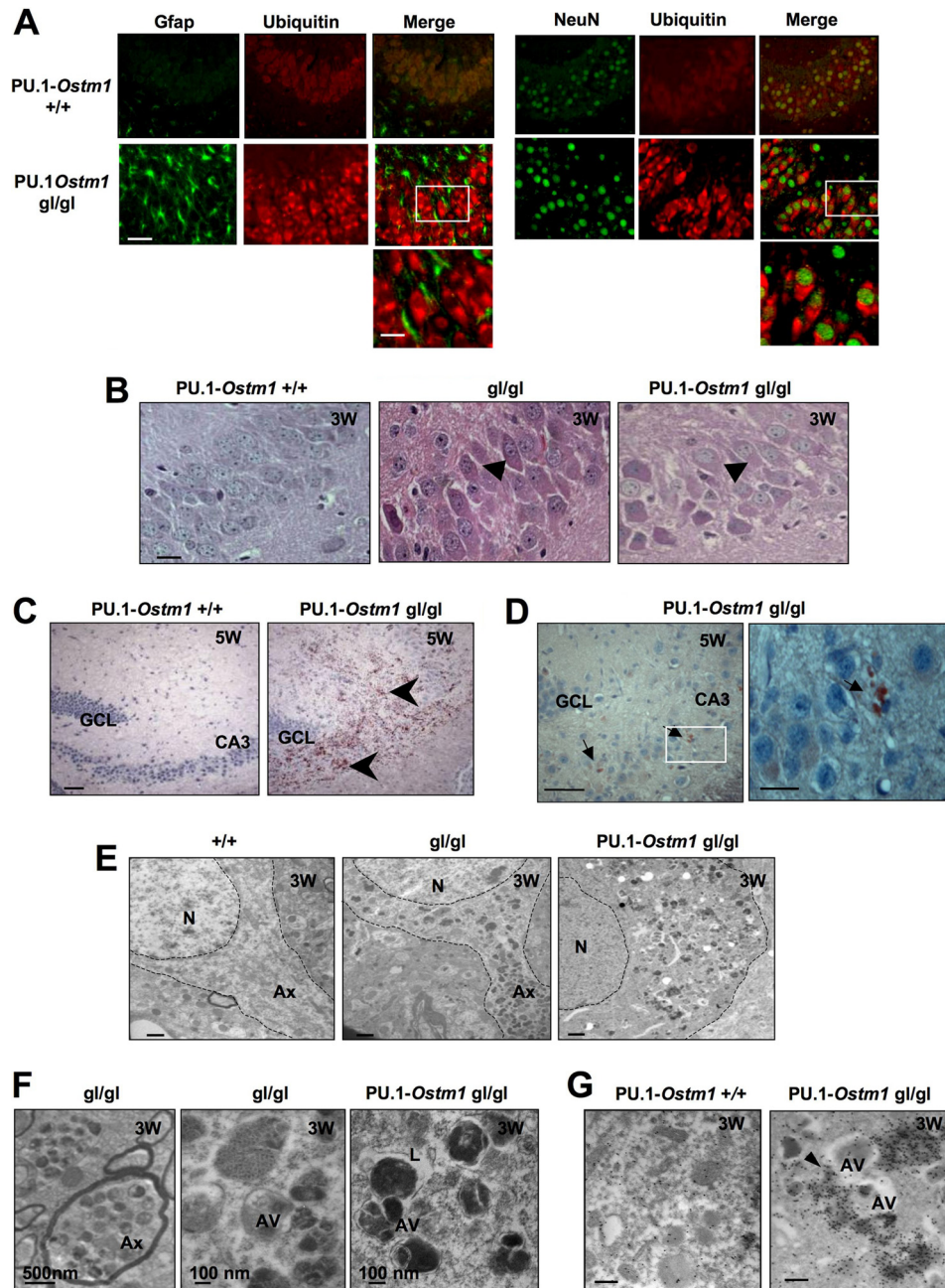
FIGURE 3. **Neuronal storage defect in PU.1-*Ostm1* gl/gl mice.** *A*, serial hippocampal sections of 4-week-old (*4W*) PU.1-*Ostm1* gl/gl mice coimmunostained with Gfap and ubiquitin (*left panels*) are negative for the presence of free and/or conjugated ubiquitin in astrocytes. In contrast, co-immunostaining with ubiquitin and NeuN (*right panels*) displayed significant accumulation of free and/or conjugated ubiquitin in pyramidal neurons from the CA3 layer compared with controls. *Scale bars*, 50 μm; 20 μm in *inset*. *B*, analysis of the CA3 layer in hippocampus from 3-week-old PU.1-*Ostm1* gl/gl in comparison with gl/gl and PU.1-*Ostm1* +/+ mice shows glycol/carbohydrate conjugates storage (*arrowheads*) in PU.1-*Ostm1* gl/gl and gl/gl compared with control (periodic acid-Schiff staining). *Scale bar*, 20 μm. *C*, hippocampus frozen sections from PU.1-*Ostm1* gl/gl mice at 5 weeks old compared with PU.1-*Ostm1* +/+ control display elevated neuronal intracellular lipid storage (*arrowheads*) by Oil Red O staining. *GCL*, granular cell layer; CA3, pyramidal cell layer. *Scale bar*, 50 μm. *D*, hippocampus paraffin-embedded sections from 5-week-old PU.1-*Ostm1* gl/gl mice exhibit extraneuronal lipid storage (*arrows*) by Oil Red O staining. *GCL*, granular cell layer; *CA3*, pyramidal cell layer. *Scale bar*, 50 μm; 20 μm in *inset*. *E*, ultrastructural analysis of 3-week-old PU.1-*Ostm1* gl/gl, gl/gl, and wild-type brain sections was examined by electron microscopy. Both PU.1-*Ostm1* gl/gl and gl/gl (*right* and *middle*) had electron-dense deposits in cortical neuron perikaryon and in swollen axons compared with control (*left*). N, nucleus; *Ax*, axon. *Scale bar*, 1 mm. *F*, higher magnification of EM axonal cross-sections (*left*) and cortical neurons (*middle* and *left*) exhibit double and single membrane vesicular structures corresponding to autophagosomal structure (*AV*) and lysosomes (*L*) in 3-week-old gl/gl and 5-week-old PU.1-*Ostm1* gl/gl mice. *AV*, autophagic vesicles; *L*, lysosome. *G*, neurons of 3-week-old PU.1-*Ostm1* gl/gl mice stained with anti-ubiquitin immunogold highlight intense accumulation of free and/or conjugated ubiquitin in autophagosomal structures. *Scale bar*, 200 nm.

drates, and lipid conjugates in PU.1-O*stm1* gl/gl mice indicates that Ostm1 plays a major role in regulating neuronal cell metabolism and suggests an impaired autophagy mechanism.

To further characterize the intracellular impact of Ostm1-associated metabolic defects, ultrastructural analyses of brain sections was undertaken in 3-week-old gl/gl and PU.1-*Ostm1* gl/gl mice. Unlike neurodegenerative disorders of the lysosomal storage subgroups, single membrane lysosomes in these mice were normal in appearance and numbers. This observation was confirmed by unaltered expression level of the lysosomal trans-
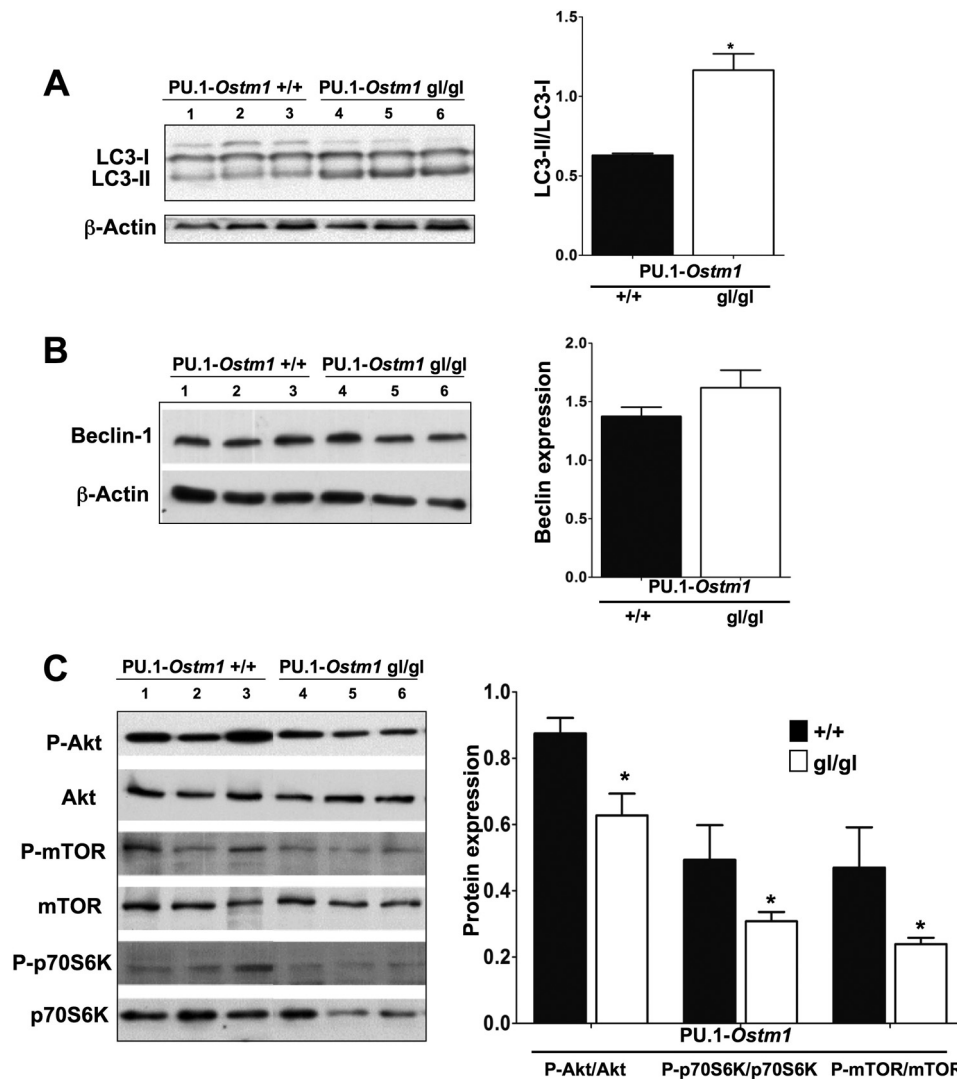
FIGURE 4. **Stimulation of the autophagy mechanism in PU.1-*Ostm1* gl/gl CNS.** *A*, brain extract analysis of three PU.1-*Ostm1* gl/gl mice (*lanes 1–3*) by Western blot displayed significant quantitative increase of LC3-II/LC3-I ratio compared with three PU.1-*Ostm1* +/+ controls (*lanes 4–6*). *, $p < 0.05$. *B*, analysis of brain extracts from three PU.1-*Ostm1* gl/gl mice (*lanes 1–3*) by Western blot denoted similar levels of Beclin-1 expression compared with three PU.1-*Ostm1* +/+ controls (*lanes 4–6*). *C*, analysis of brain extracts of 3-week-old PU.1-*Ostm1* gl/gl mice (*lanes 1–3*) displayed significantly decreased expression levels throughout the mTOR signaling cascade, including active phospho-mTOR (*P-mTOR*), phospho-Akt (*p-Akt*), and downstream effector phospho-p70S6K (*P-p70S6K*), in comparison with three PU.1-*Ostm1* +/+ controls (*lanes 4–6*). *, $p < 0.05$. *Error bars*, S.E.

membrane structural proteins Lamp1 and Lamp2 and by unnoticeable autofluorescence (data not shown) that differs from neuronal ceroid lipofuscinosis lysosomal storage disorders (20). In contrast, there was an important accumulation of numerous electron-dense inclusions in neuronal perikaryon and cytosol (Fig. 3*E*). Such accumulation extended into the axons of cortical and hippocampal neurons, frequently causing axonal swelling (Fig. 3*E*). Importantly, higher magnification of PU.1-*Ostm1* gl/gl neuronal sections, similar to gl/gl, revealed that these inclusions consisted predominantly of double membrane vesicular structures typical of autophagosomes (Fig. 3*F*). With advancing age, autophagosome accumulation was further exacerbated in PU.1-*Ostm1* gl/gl mice. To identify whether these neuronal autophagosome inclusions are composed of ubiquitin-targeted substrates, anti-ubiquitin immunogold staining was performed on PU.1-*Ostm1* gl/gl sections. Most of the cytoplasmic osmophilic inclusions were ubiquitin-positive, consistent with large protein accumulation in autophagosomes (Fig. 3*G*). This early response of

Ostm1-defective cell metabolism with protein, carbohydrate, and lipid accumulation is concomitant with the formation of autophagosomal structures in neurons, possibly as a protective response that precedes massive neurodegeneration.

Induction of an Enhanced Autophagic Response in the Absence of Ostm1—Based on the abundance of autophagic vesicles in PU.1-*Ostm1* gl/gl neuronal cells detected by electron microscopy, stimulation of the autophagy pathway was monitored in the CNS of gl/gl and PU.1-*Ostm1* gl/gl mice using specific autophagic molecular markers and signaling effectors. The expression ratio of the autophagosomal lipidated form of LC3 (LC3-II) relative to cytosolic LC3-I was monitored using Western blot analyses of total brain protein extracts. In PU.1-*Ostm1* gl/gl lysates, this ratio was significantly increased (by ~1.8-fold) compared with controls by 3 weeks of age (Fig. 4*A*). This result is significant, considering that neurons constitute a minor fraction of the brain cell population, and further shows accumulation of autophagosomes, consistent with our cellular EM analyses (Fig. 3, *E–G*).

To investigate the Ostm1 autophagy signaling cascade in the neurodegeneration of PU.1-*Ostm1* gl/gl mice, the two pathways normally associated with autophagy, Beclin 1 and Akt/mammalian target of rapamycin (mTOR), were analyzed. Although similar expression of Beclin-1 was detected in PU.1-*Ostm1* gl/gl total brain protein extracts compared with controls (Fig. 4*B*), modulation of the mTOR pathway was evidenced by a significant reduction of ~30 and ~40% in activated phospho-Akt and phospho-mTOR, respectively, in PU.1-*Ostm1* gl/gl brain samples (Fig. 4*C*). This modulation further correlated with an ~50% decrease in activation of the mTOR target phospho-p70S6K kinase (Fig. 4*C*), consistent with observations in Huntington's disease (21). These data indicate overall inhibition of the neuronal mTOR pathway in PU.1-*Ostm1* gl/gl mice that results in stimulation of autophagy, consistent with accumulation of autophagosomes and probably ineffective clearance by the unstimulated lysosomal compartment. Therefore, build-up of proteins, carbohydrates, and lipids in Ostm1-null neurons deregulate the autophagy mechanism and actively contribute to neuronal cell loss.

CNS Defects Persist with Ostm1 Astrocyte-specific Expression—Because it has been shown that astrocytes can play a role in neuronal disease progression and/or protection (22, 23), we directly addressed whether Ostm1-deficient astrocytes contribute to the PU.1-*Ostm1* gl/gl neurodegeneration via a complementation strategy. Three transgenic hGFAP-*Ostm1* mouse lines were generated by specifically targeting Ostm1 expression in astrocytes using the human hGFAP promotor (24) (Fig. 5*A*) and were analyzed for expression. As shown in Fig. 5*B*, one of the hGFAP-*Ostm1* transgenic lines showed enhanced Ostm1 levels in total transgenic brain tissue as well as in transgenic primary astrocyte cells compared with controls (Fig. 5*B*). Transgenic hGFAP-*Ostm1* mice developed normally and did not display any abnormal phenotype. We produced hGFAP-*Ostm1*-PU.1-*Ostm1* gl/gl mice by successive matings to gl/+ mice. Analyses of these double transgenics on gl/gl background at 6–7 weeks of age displayed a major loss of neurons in the CA3 layer of hippocampus, atrophy of the cerebral cortex and corpus callosum, enlargement of the lateral ventricles, and severe astrogliosis (Fig. 5, *C* and *D*). In addition, the neuronal autophagic responses determined by the LC3-II/LC3-I and phospho-mTOR/mTOR CNS ratios were significantly increased and decreased, respectively, in these mice and comparable with that detected in PU.1-*Ostm1* gl/gl mice (Fig. 5*E*). The double hGFAP-*Ostm1*-PU.1-*Ostm1* gl/gl transgenic mice had a similar lifespan and phenotype as the PU.1-*Ostm1* gl/gl transgenic mice. The Ostm1 astrocyte inflammatory response could correspond to an indirect role in the neurodegeneration process.

Ostm1 Autonomous Role in Neuronal Degeneration—Because neuronal loss in PU.1-*Ostm1* gl/gl does not result from a unique defective glial cellular compartment, we investigated whether Ostm1 has an intrinsic role in neurons alone or in both glial and neuronal cells. Using a similar complementation strategy as for astrocytes, we produced transgenic mice that specifically targeted *Ostm1* expression in neurons using the rat synapsin 1 (Syn1) gene promotor (25). Two Syn1-*Ostm1* transgenic mouse lines (2 and 10 copies of the transgene) (Fig. 6*A*) were generated and exhibited brain-specific expression of the transgene based on qPCR (Fig. 6*B*). Because these mice did not display any abnormal phenotype, each mouse line was first crossed to gl/+ mice to generate Syn1-*Osm1* gl/+ mice and subsequently to PU1-*Ostm1* gl/+ mice to generate double transgenic Syn1-*Ostm1*-PU.1-*Ostm1* gl/gl progeny to test for phenotypic rescue *in vivo*. The low and high Syn1-*Ostm1* expressors were mated to PU.1-*Ostm1* lines (11), and each line of double transgenic gl/gl mice showed the same phenotype. In contrast to the severe neurodegeneration detected by MRI in 6-week-old (*6W*) single PU.1-*Ostm1* gl/gl transgenic mice, all double Syn1-*Ostm1*-PU.1-*Ostm1* gl/gl transgenic progeny exhibit a CNS structure indistinguishable from controls (Fig. 6*C*). The functional rescue also included the hippocampus, cortex, and retina that showed normal distribution of inner and outer photoreceptor segments in double transgenics relative to the severe degeneration observed in single PU.1-*Ostm1* gl/gl transgenic mice (Figs. 2 (*A–D*) and 6*E*). Complementation of the neuronal autophagic response was also observed, with LC3-II/LC3-I and phospho-mTOR/mTOR ratios reaching basal control levels in double Syn1-*Ostm1*-PU.1-*Ostm1* gl/gl transgenic mice (Fig. 6*F*). Noticeably, these double transgenic mice had an absence of astrogliosis, indicating that the CNS inflammatory response arises as a secondary mechanism. Consistently, the Syn1-*Ostm1*-PU.1-*Ostm1* gl/gl transgenic mice had normal lifespan expectancy. The single Syn1-*Ostm1* gl/gl transgenic mice showed appropriate CNS structural organization but died by ~3 weeks of age from hematopoietic defects, similar to the gl/gl mice (Fig. 6*D*). These results demonstrate full rescue of Ostm1-associated neurodegeneration in double Syn1-*Ostm1*-PU.1-*Ostm1* gl/gl transgenic mice.

DISCUSSION

This study establishes that Ostm1 in the CNS plays an essential role in neurons, as shown by extensive and severe neurodegeneration in null mice. This function of Ostm1 was revealed by the limited increased lifespan upon functional rescue of hematopoietic lineage defects. Ostm1-deficient CNS first developed gliosis with increased astrocyte cell population and microglia activation in parallel with retinal degeneration at 2–3 weeks of age. Within 1 week, the phenotype progressed to a widespread and marked neuronal cell metabolic defect with autophagosome accumulation via the mTOR pathway. Subsequent to autophagy stimulation, these mice demonstrated swift and massive neurodegeneration and brain atrophy that resulted in premature death at a median age of 5.4 weeks. Moreover, our analyses of specific targeted transgenic expression in distinct CNS cell subpopulations determined that Ostm1 has a primary and autonomous role in neuron homeostasis. Thus, the direct role of Ostm1 in CNS neurons correlates with our patient studies and reveals Ostm1 as a potential key effector or modulator in different neuropathologies.

Evidence of histopathologic inflammation with microglia activation and an increased astrocyte population indicates a primary role or an indirect functional cellular physiologic response induced by the loss of Ostm1. The microglia-increased inflammation in the osteopetrosis-rescued PU.1-*Ostm1* gl/gl at 3 weeks of age, similar to the gl/gl mice, sug-
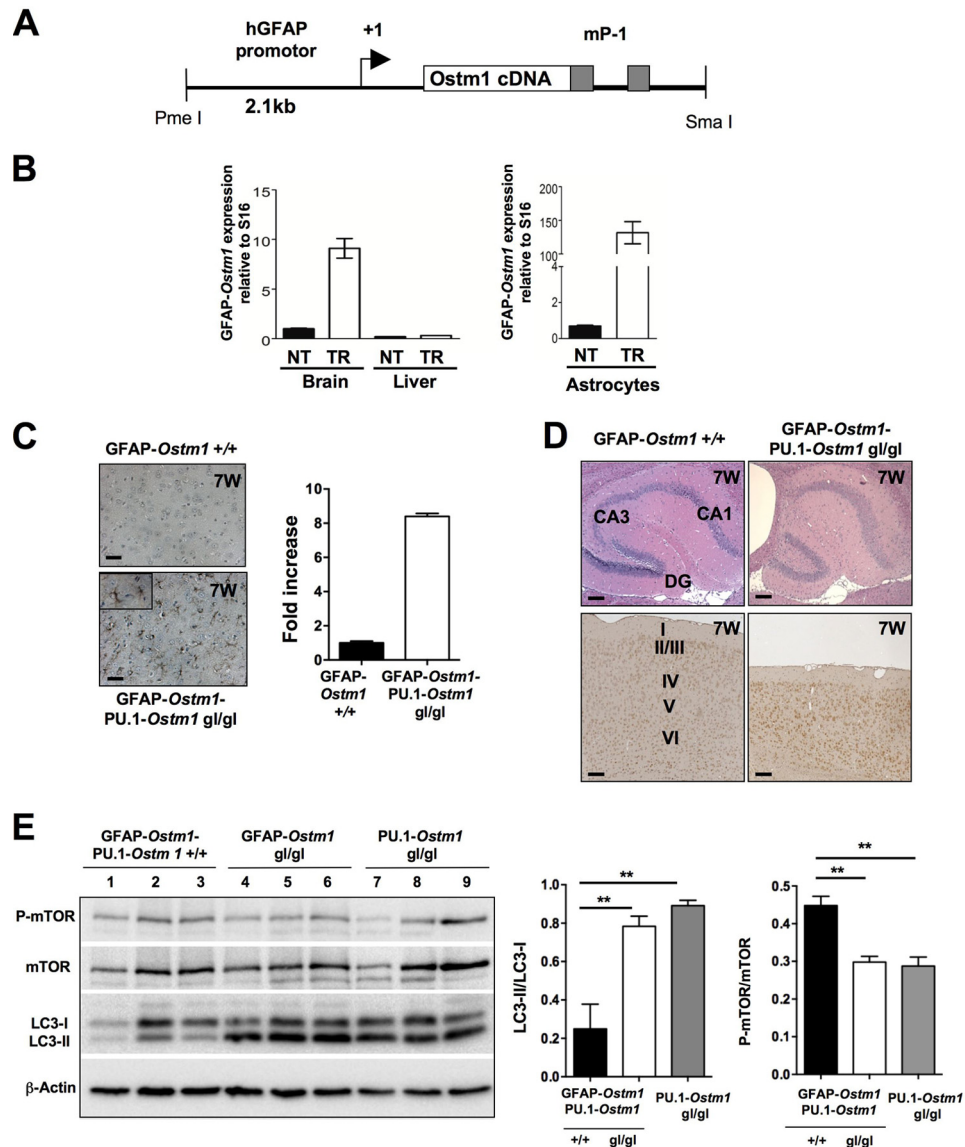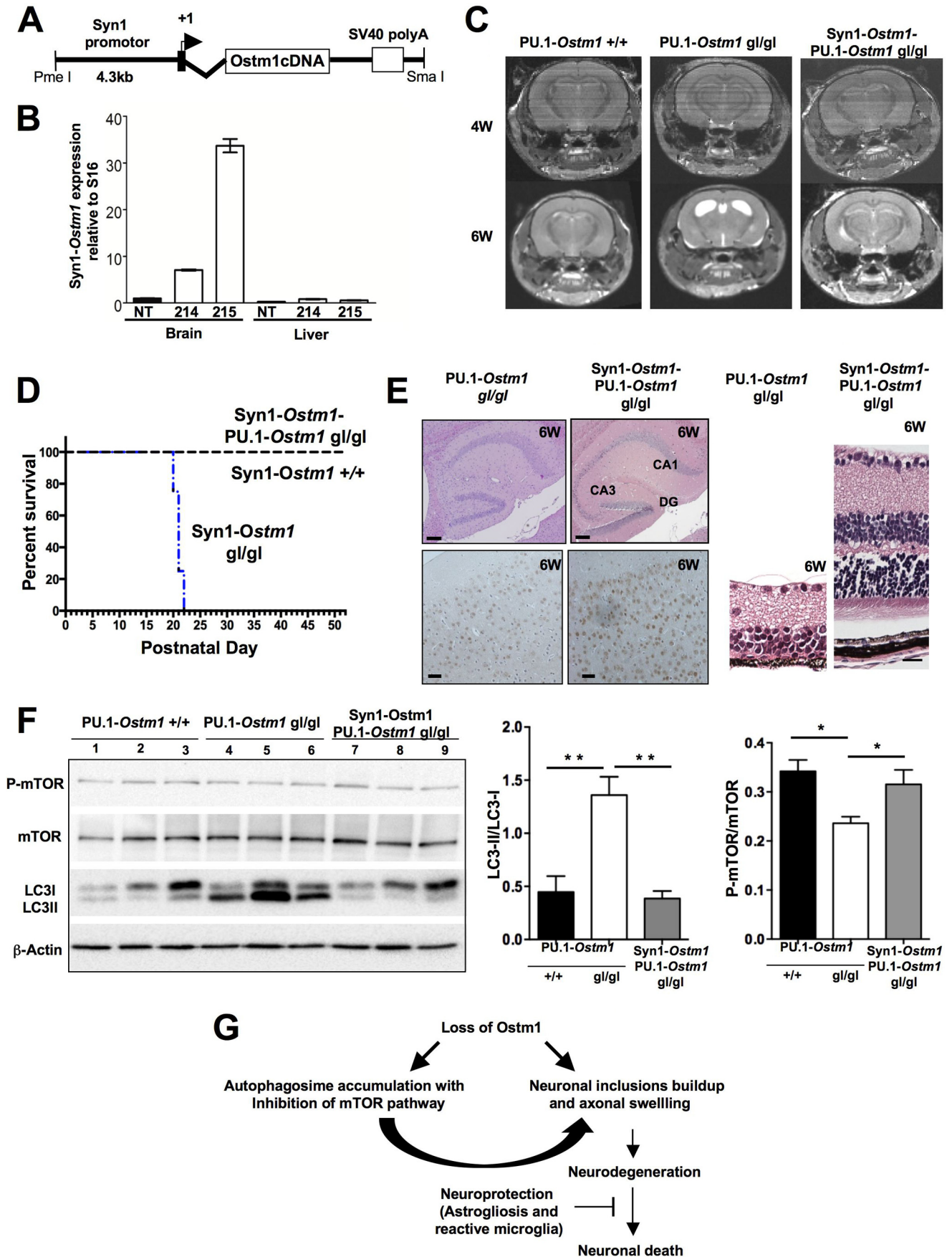
FIGURE 5. **Neurodegeneration persists with Ostm1 targeted to astrocytes.** *A*, representation of the transgene used to generate hGFAP-*Ostm1* mice. The human GFAP regulatory sequence (*hGFAP*) from −2,163 to +47 was cloned upstream of the *Ostm1* (1.055 kb) open reading frame, followed by an intron and poly(A) signal of the mouse protamine-1 gene (*mP-1*). *B*, expression analysis of the GFAP-*Ostm1* transgene (*TR*) relative to non-transgenic (*NT*) in total brain and liver as tissue control (*left*) and enriched primary astrocytes (*right*). Expression is relative to S16 as internal control. *C*, analysis of cerebral cortex from double hGFAP-*Ostm1*-PU.1-*Ostm1* gl/gl transgenic mice (*n* = 6) relative to hGFAP-*Ostm1* +/+ controls by Gfap immunostaining (*left panels*) exhibits significant stimulation of astrogliosis (∼7-fold; *right*). *Scale bar*, 50 μm. *D*, severe neurodegeneration in 7-week-old double hGFAP-*Ostm1*-PU.1-*Ostm1* gl/gl transgenic mice (*right*) compared with single hGFAP-*Ostm1* +/+ transgenic control (*left*). The hGFAP-*Ostm1*-PU.1-*Ostm1* gl/gl sections displayed loss of CA3 hippocampus cell layer (*top panels*, H&E staining; *scale bar*, 1 mm) and decreased cerebral cortex thickness by NeuN immunostaining (*bottom panels*; *scale bar*, 50 μm). *E*, Western blots and histograms of the LC3-II/LC3-I and phospho-mTOR (*P-mTOR*)/mTOR ratios from brain extracts of GFAP-*Ostm1*-PU.1-*Ostm1* +/+ (*lanes 1–3*), GFAP-*Ostm1gl/gl* (*lanes 4–6*), and PU.1-*Ostm1* gl/gl mice (*lanes 7–9*). From Western blot quantification, the GFAP-*Ostm1* gl/gl and PU.I-*Ostm1* gl/gl mice show a similar increase in the LC3-II/LC3-I and decrease in phospho-mTOR/mTOR ratios, compared with GFAP-Ostm1-PU.1-Ostm1 +/+ controls. **, $p < 0.01$. *Error bars*, S.E.

gested that this process most likely results from a secondary reaction because Ostm1 is expressed in microglia. Prominent stimulation of the astrocyte cell population parallels expansion of hematopoietic macrophages and osteoclast cell populations upon loss of Ostm1 function (11). Accordingly, Ostm1 appears to be a negative modulator of cell proliferation. Such activation of astrocytes could be directly responsible for neuronal death by increased toxicity (26). Alternatively, astrogliosis could be a consequence of neuronal loss. In addition to this inflammation, photoreceptor degeneration in the retina of 3-week-old gl/gl and PU.1-*Ostm1* gl/gl mice revealed a genuine role for Ostm1 in

the retina that is not secondary to excess bone from gradual occlusion of skull foramina. Fulgurant neuronal loss in the next 2 weeks occurred in all regions of the PU.1-*Ostm1* gl/gl brain and resulted in major neurodegeneration with cerebral atrophy. This finding highlights lower susceptibility in the hippocampus, cortex, and cerebellum relative to retina upon absence of Ostm1. This difference suggests the existence of a factor with partially redundant function to Ostm1 in the brain relative to the retina or a greater protective role of astrocytes that delay disease progression in the brain, as in amyotrophic lateral sclerosis (22). Consistently, astrogliosis and CNS inflam-

matory response prior to acute neuronal loss is frequent in several human neurodegenerative diseases (27) but could also be responsible for the phenotype.

Based on molecular and cellular characteristics, the absence of Ostm1 resulted in a distinct type of brain disorder. Accumulation of cellular ubiquitin in the neurons specifically of PU.1-*Ostm1* gl/gl mice suggested protein misfolding or misprocessing. Such mechanisms occur in many types of human neurodegeneration, such as mucolipidosis and Huntington, Parkinson, and Alzheimer diseases (20). Altered cell metabolism in Ostm1 null neurons, with intracellular storage of ubiquitinated proteins, carbohydrates, and lipids from most regions of the brain, was concomitant with the presence of numerous electron-dense, double-membrane vesicular structures or autophagosomes. This autophagic response in Ostm1-deficient brains correlated with increased LC3II/LC3I and decreased phospho-mTOR/mTOR ratios. The accumulation of autophagosomes was so severe that it resulted in axonal swelling. Similar features with impaired vesicular trafficking were characterized in the dynactin/dynein motor mouse mutants and in Alzheimer disease mouse models (28–31). Evidence for stimulation of autophagy is provided by significant down-regulation of the mTOR pathway. Consistently, both the downstream target phospho-p70S6K and phospho-Akt are also repressed in Ostm1-deficient brains (32). Of interest, the accumulation of autophagosomes was most likely exacerbated by the unstimulated lysosomal compartment, determined from the unchanged transmembrane Lamp1 and Lamp2 protein levels. This supports a potential role for *Ostm1* upstream of the lysosomal compartment, such as endolysosomal transport on microtubules or in the fusion of autophagosome with lysosomes to form autophagolysosomes (33). Nonetheless, the accumulation of autophagosomes in the absence of Ostm1 appears to result from both enhanced autophagy and unstimulated lysosomal degradation process. Hence, this impaired physiologic sequence in the autophagy to lysosomal mechanism leads to massive CNS neuronal loss (Fig. 6*F*).

Neurodegeneration arises in a number of mouse mutants. The Ostm1 mouse mutant has some similarities with the autophagy gene *Atg5* and *Atg7* null mice (34, 35), the lysosomal enzyme Cln3$^{\Delta ex7/8}$ (36) and cathepsin D null mice (37), and the chloride channel ClC7 null mice (14), all of which have an accumulation of toxic metabolites. The Cln3$^{\Delta ex7/8}$ and cathepsin D null mice like PU.1-*Ostm1* gl/gl showed activation of the mTOR-dependent and Beclin-1-independent autophagic signaling pathways but with evidence of autofluorescence as in a lysosomal storage disease. ClC7 null neurons display increased carbohydrates in lysosomes (38, 39) with pronounced autofluo-

rescence, a hallmark of neuronal ceroid lipofuscinosis (40). In Ostm1 null neurons, accumulation of lipids and carbohydrates is, however, detected in autophagosomes without lysosomal autofluorescence that differs from the ClC7 typical lysosomal storage disease. Further, the neurodegeneration in the PU.1-*Ostm1* gl/gl transgenic mouse model is much more severe and leads to a shorter lifespan than the ClC7 null and forebrain-conditional mice (16) or even the Cln3$^{\Delta ex7/8}$ and cathepsin D null mice. The earlier onset and more severe progression of Ostm1 phenotype in comparison with CLC7 suggest additional functions of Ostm1 and/or the existence of other interacting partners.

The implication of microglia, astrocytes, and neurons in Ostm1 brain pathology indicates that Ostm1 could be important in only one cell type or in a combination of these cell types, as observed for multiple hematopoietic lineages (11). Given that specific microglial Ostm1 transgene expression in null Ostm1 mice did not improve the CNS pathology, the phenotype is either a secondary event or involves Ostm1 in both microglia and another cell type. Analyses of the role of astrocytes revealed that astrocyte-targeted Ostm1 expression in Ostm1-deficient brain was insufficient by itself to rescue the phenotype or delay neuronal death. This result supports two possibilities: 1) Ostm1 could play a direct role in astrocytes conjointly with an additional cell type, or 2) astrogliosis is in response to neuronal cell death for functional protection. The critical role of Ostm1 in neurons was highlighted by complete rescue of the CNS defects in Ostm1-deficient brain with specific neuron-targeted expression of *Ostm1*. Full correction of the phenotype, including astrogliosis and microgliosis, demonstrates that Ostm1 plays a cell-autonomous role in neurons and excludes a primary role for Ostm1 in astrocytes as responsible for neurodegeneration. Thus, Ostm1 appears to directly target the neurons rather than a combination of cells in the CNS.

Among the different types of human neurodegenerative disorders, Ostm1/OSTM1 pathology shares many typical features with known subclasses. Importantly, the accumulation of proteins, as well as carbohydrate and lipid conjugates, in Ostm1 neurons is also detected in Huntington, Parkinson, and Alzheimer diseases as well as in a few subgroups of human lysosomal storage deficiencies (mucolipidosis, Niemann-Pick type C, and Danon disease) (20, 41, 42). Molecular and histopathological analyses in the Ostm1-deficient mice showed many common traits with Alzheimer disease, including an enhanced autophagic response (43), metabolic defects, and axonal swelling. At present, Ostm1-distinct characteristics cannot be attributed to a particular neurodegeneration subclass. Nonetheless, Ostm1 neurodegenerative disorder mirrors the

FIGURE 6. **Neurodegenerative rescue in Syn1-*Ostm1*-PU.1-*Ostm1* gl/gl transgenic mice.** *A*, representation of the transgene used to generate Syn1-*Ostm1* mice. The rat Syn1 promotor (4.3 kb) was cloned upstream of the *Ostm1* (1.055 kb) open reading frame, followed by the 240-bp SV40 poly(A) signal. *B*, brain quantitative transgene (*TR*) expression for Syn1-*Ostm1* transgenic lines compared with non-transgenic (*NT*) controls. Liver was used as tissue control, and S16 was used as internal control. *C*, MRI brain scans from 4- (*4W*) and 6-week-old (*6W*) PU.1-Ostm1 gl/gl (*middle panels*), Syn1-*Ostm1*-PU.1-*Ostm1* gl/gl (*right panels*), and control wild type (*left panels*) mice. Syn1-*Ostm1*-PU.1-*Ostm1* gl/gl displayed complete correction of the CNS defects observed in the PU.1-Ostm1 gl/gl and is indistinguishable from wild type controls. *D*, Kaplan-Meier curve of PU.1-*Ostm1*-Syn1-*Ostm1* gl/gl mice (n = 8) compared with Syn-*Ostm1* gl/gl (n = 5) and Syn-*Ostm1* +/+ (n = 8) control mice. *E*, normal hippocampus, cortex (*left panels*) and retinal (*right panels*) histologic structures in double transgenic Syn1-*Ostm1*-PU.1-*Ostm1* gl/gl mice compared with severe degeneration in 6-week-old PU.1-*Ostm1* gl/gl mice. (H&E staining, *scale bar*, 1 mm; Neu N immunostaining, *scale bar*, 50 μm). *F*, autophagy stimulation in PU.1-*Ostm11* gl/gl (*lanes 4–6*) is abrogated in the Syn1-*Ostm1*-PU.1-*Ostm1* gl/gl mice (*lanes 7–9*), as shown by the LC3-II/LC3-I and phospho-mTOR/mTOR ratios similar to PU.1-*Ostm1* +/+ controls (*lanes 1–3*). *G*, proposed model of *Ostm1*-mediated neuronal dysfunction leading to neurodegeneration. *, p < 0.05; **, p < 0.01. Error bars, S.E.

Ostm1 and Neuronal Homeostasis

OSTM1 osteopetrotic patients. Indeed, both the mouse and human phenotypes display cerebral atrophy, retinal degeneration, gliosis, and demyelination and die at an early age (~5 weeks in the mice and in the first year in humans) (3–5, 7, 9, 44). The Ostm1 null mouse is thus a *bona fide* orthologous neurodegenerative model. The clinical implications of these findings indicate that bone marrow transplantation therapy for the OSTM1 patients with severe osteopetrosis and altered hematopoiesis is most likely unsuitable because these individuals are susceptible to CNS neurodegeneration (45).

Our characterization of severe and extensive neurodegeneration in Ostm1-deficient brains independently of hematopoietic defects identified an essential factor in neuronal homeostasis and physiology. Ostm1 plays a key function in the intracellular trafficking mechanism of organelles in the late endosome, autophagosome, and lysosome cascade. Importantly, we demonstrated a neuronal cell-autonomous role for Ostm1 in CNS pathology that indirectly induced axonal swelling and widespread inflammatory gliosis. In summary, these mice provide a highly relevant model to understand and alleviate the molecular pathologic mechanism of this disorder and potentially neurodegeneration-related diseases.

REFERENCES

1. Tolar, J., Teitelbaum, S. L., and Orchard, P. J. (2004) Osteopetrosis. *N. Engl. J. Med.* **351,** 2839–2849
2. Steward, C. G. (2003) Neurological aspects of osteopetrosis. *Neuropathol. Appl. Neurobiol.* **29,** 87–97
3. Quarello, P., Forni, M., Barberis, L., Defilippi, C., Campagnoli, M. F., Silvestro, L., Frattini, A., Chalhoub, N., Vacher, J., and Ramenghi, U. (2004) Severe malignant osteopetrosis due to a Gl gene mutation. *J. Bone Miner. Res.* **19,** 1194–1199
4. Pangrazio, A., Poliani, P. L., Megarbane, A., Lefranc, G., Lanino, E., Di Rocco, M., Rucci, F., Lucchini, F., Ravanini, M., Facchetti, F., Abinun, M., Vezzoni, P., Villa, A., and Frattini, A. (2006) Mutations in OSTM1 (Grey Lethal) define a particularly severe form of autosomal recessive osteopetrosis with neural involvement. *J. Bone Miner. Res.* **21,** 1098–1105
5. Maranda, B., Chabot, G., Décarie, J.-C., Pata, M., Azeddine, B., Moreau, A., and Vacher, J. (2008) Clinical and cellular manifestations of OSTM1 related infantile osteopetrosis. *J. Bone Miner. Res.* **23,** 296–300
6. Castellano Chiodo, D., DiRocco, M., Gandolfo, C., Morana, G., Buzzi, D., and Rossi, A. (2007) Neuroimaging findings in malignant infantile osteopetrosis due to OSTM1 mutations. *Neuropediatrics* **38,** 154–156
7. Ott, C. E., Fischer, B., Schröter, P., Richter, R., Gupta, N., Verma, N., Kabra, M., Mundlos, S., Rajab, A., Neitzel, H., and Kornak, U. (2013) Severe neuronopathic autosomal recessive osteopetrosis due to homozygous deletions affecting OSTM1. *Bone* **55,** 292–297
8. Chalhoub, N., Benachenhou, N., Rajapurohitam, V., Pata, M., Ferron, M., Frattini, A., Villa, A., and Vacher, J. (2003) Grey-lethal mutation induces severe malignant autosomal recessive osteopetrosis in mouse and human. *Nat. Med.* **9,** 399–406
9. Mazzolari, E., Forino, C., Razza, A., Porta, F., Villa, A., and Notarangelo, L. D. (2009) A single-center experience in 20 patients with infantile malignant osteopetrosis. *Am. J. Hematol.* **84,** 473–479
10. Rajapurohitam, V., Chalhoub, N., Benachenhou, N., Neff, L., Baron, R., and Vacher, J. (2001) The mouse osteopetrotic grey-lethal mutation induces a defect in osteoclast maturation/function. *Bone* **28,** 513–523
11. Pata, M., Héraud, C., and Vacher, J. (2008) OSTM1 bone defect reveals an intercellular hematopoietic crosstalk. *J. Biol. Chem.* **283,** 30522–30530
12. Lange, P. F., Wartosch, L., Jentsch, T. J., and Fuhrmann, J. C. (2006) ClC-7 requires Ostm1 as a β-subunit to support bone resorption and lysosomal function. *Nature* **440,** 220–223
13. Leisle, L., Ludwig, C. F., Wagner, F. A., Jentsch, T. J., and Stauber, T. (2011) ClC-7 is a slowly voltage-gated 2Cl(−)/1H(+)-exchanger and requires Ostm1 for transport activity. *EMBO J.* **30,** 2140–2152
14. Kasper, D., Planells-Cases, R., Fuhrmann, J. C., Scheel, O., Zeitz, O., Ruether, K., Schmitt, A., Poët, M., Steinfeld, R., Schweizer, M., Kornak, U., and Jentsch, T. J. (2005) Loss of the chloride channel ClC-7 leads to lysosomal storage disease and neurodegeneration. *EMBO J.* **24,** 1079–1091
15. Kornak, U., Kasper, D., Bösl, M. R., Kaiser, E., Schweizer, M., Schulz, A., Friedrich, W., Delling, G., and Jentsch, T. J. (2001) Loss of the ClC-7 chloride channel leads to osteopetrosis in mice and man. *Cell* **104,** 205–215
16. Wartosch, L., Fuhrmann, J. C., Schweizer, M., Stauber, T., and Jentsch, T. J. (2009) Lysosomal degradation of endocytosed proteins depends on the chloride transport protein ClC-7. *FASEB J.* **23,** 4056–4068
17. Ginhoux, F., Greter, M., Leboeuf, M., Nandi, S., See, P., Gokhan, S., Mehler, M. F., Conway, S. J., Ng, L. G., Stanley, E. R., Samokhvalov, I. M., and Merad, M. (2010) Fate mapping analysis reveals that adult microglia derive from primitive macrophages. *Science* **330,** 841–845
18. Levine, B., and Kroemer, G. (2008) Autophagy in the pathogenesis of disease. *Cell* **132,** 27–42
19. Martinez-Vicente, M., and Cuervo, A. M. (2007) Autophagy and neurodegeneration: when the cleaning crew goes on strike. *Lancet Neurol.* **6,** 352–361
20. Platt, F. M., Boland, B., and van der Spoel, A. C. (2012) Lysosomal storage disorders: the cellular impact of lysosomal dysfunction. *J. Cell Biol.* **199,** 723–734
21. Ravikumar, B., Vacher, C., Berger, Z., Davies, J. E., Luo, S., Oroz, L. G., Scaravilli, F., Easton, D. F., Duden, R., O'Kane, C. J., and Rubinsztein, D. C. (2004) Inhibition of mTOR induces autophagy and reduces toxicity of polyglutamine expansions in fly and mouse models of Huntington disease. *Nat. Genet.* **36,** 585–595
22. Yamanaka, K., Chun, S. J., Boillee, S., Fujimori-Tonou, N., Yamashita, H., Gutmann, D. H., Takahashi, R., Misawa, H., and Cleveland, D. W. (2008) Astrocytes as determinants of disease progression in inherited amyotrophic lateral sclerosis. *Nat. Neurosci.* **11,** 251–253
23. Vargas, M. R., Johnson, D. A., Sirkis, D. W., Messing, A., and Johnson, J. A. (2008) Nrf2 activation in astrocytes protects against neurodegeneration in mouse models of familial amyotrophic lateral sclerosis. *J. Neurosci.* **28,** 13574–13581
24. Brenner, M., Kisseberth, W. C., Su, Y., Besnard, F., and Messing, A. (1994) GFAP promotor directs astrocyte-specific expression in transgenic mice. *J. Neurosci.* **14,** 1030–1037
25. de Luca, C., Kowalski, T. J., Zhang, Y., Elmquist, J. K., Lee, C., Kilimann, M. W., Ludwig, T., Liu, S.-M., and Chua, S. C., Jr. (2005) Complete rescue of obesity, diabetes, and infertility in db/db mice by neuron-specific LEPR-B transgenes. *J. Clin. Invest.* **115,** 3484–3493
26. Rodríguez, J. J., Olabarria, M., Chvatal, A., and Verkhratsky, A. (2009) Astroglia in dementia and Alzheimer's disease. *Cell Death Differ.* **16,** 378–385
27. Wada, R., Tifft, C. J., and Proia, R. L. (2000) Microglial activation precedes acute neurodegeneration in Sandhoff disease and is suppressed by bone marrow transplantation. *Proc. Natl. Acad. Sci. U.S.A.* **97,** 10954–10959
28. Laird, F. M., Farah, M. H., Ackerley, S., Hoke, A., Maragakis, N., Rothstein, J. D., Griffin, J., Price, D. L., Martin, L. J., and Wong, P. C. (2008) Motor neuron disease occurring in a mutant dynactin mouse model is characterized by defects in vesicular trafficking. *J. Neurosci.* **28,** 1997–2005
29. Nixon, R. A. (2007) Autophagy, amyloidogenesis and Alzheimer disease. *J. Cell Sci.* **120,** 4081–4091
30. Lee, S., Sato, Y., and Nixon, R. A. (2011) Lysosomal proteolysis selectively disrupts axonal transport of degradative organelles and causes an Alzheimer's-like axonal dystrophy. *J. Neurosci.* **31,** 7817–7830
31. Millecamps, S., and Julien, J.-P. (2013) Axonal transport deficits and neurodegenerative diseases. *Nat. Rev. Neurosci.* **14,** 161–176

32. Klionsky, D. J., and Emr, S. D. (2000) Autophagy as a regulated pathway of cellular degradation. *Science* **290,** 1717–1721

33. Mizushima, N., Yamamoto, A., Hatano, M., Kobayashi, Y., Kabeya, Y., Suzuki, K., Tokuhisa, T., Ohsumi, Y., and Yoshimori, T. (2001) Dissection of autophagosome formation using Atg5-deficient mouse embryonic stem cells. *J. Cell Biol.* **152,** 657–668

34. Hara, T., Nakamura, K., Matsui, M., Yamamoto, A., Nakahara, Y., Suzuki-Migishima, R., Yokoyama, M., Mishima, K., Saito, I., Okano, H., and Mizushima, N. (2006) Suppression of basal autophagy in neuronal cells causes neurodegenerative disease in mice. *Nature* **441,** 885–889

35. Komatsu, M., Waguri, S., Chiba, T., Murata, S., Iwata, J., Tanida, I., Ueno, T., Koike, M., Uchiyama, Y., Kominami, E., and Tanaka, K. (2006) Loss of autophagy in the central nervous system causes neurodegeneration in mice. *Nature* **441,** 880–884

36. Cao, Y., Espinola, J. A., Fossale, E., Massey, A. C., Cuervo, A. M., MacDonald, M. E., and Cotman, S. L. (2006) Autophagy is disrupted in a knock-in mouse model of juvenile neuronal ceroid lipofuscinosis. *J. Biol. Chem.* **281,** 20483–20493

37. Koike, M., Shibata, M., Waguri, S., Yoshimura, K., Tanida, I., Kominami, E., Gotow, T., Peters, C., von Figura, K., Mizushima, N., Saftig, P., and Uchiyama, Y. (2005) Participation of autophagy in storage of lysosomes in neurons from mouse models of neuronal ceroid-lipofuscinoses (Batten disease). *Am. J. Pathol.* **167,** 1713–1728

38. Poët, M., Kornak, U., Schweizer, M., Zdebik, A. A., Scheel, O., Hoelter, S., Wurst, W., Schmitt, A., Fuhrmann, J. C., Planells-Cases, R., Mole, S. E., Hübner, C. A., and Jentsch, T. J. (2006) Lysosomal storage disease upon disruption of the neuronal chloride transport protein ClC-6. *Proc. Natl. Acad. Sci. U.S.A.* **103,** 13854–13859

39. Pressey, S. N., O'Donnell, K. J., Stauber, T., Fuhrmann, J. C., Tyynelä, J., Jentsch, T. J., and Cooper, J. D. (2010) Distinct neuropathologic phenotypes after disrupting the chloride transport proteinc ClC-6 and ClC-7/Ostm1. *J. Neuropathol. Exp. Neurol.* **69,** 1228–1246

40. Goebel, H. H., and Wisniewski, K. E. (2004) Current state of clinical and morphological features in human NCL. *Brain Pathol.* **14,** 61–69

41. Pacheco, C. D., Kunkel, R., and Lieberman, A. P. (2007) Autophagy in Niemann-Pick C disease is dependent upon beclin-1 and responsive to lipid trafficking defects. *Hum. Mol. Genet.* **16,** 1495–1503

42. Prinetti, A., Rocchetta, F., Costantino, E., Frattini, A., Caldana, E., Rucci, F., Bettiga, A., Poliani, P. L., Chigorno, V., and Sonnino, S. (2009) Brain lipid composition in grey-lethal mutant mouse characterized by severe malignant osteopetrosis. *Glycoconj. J.* **26,** 623–633

43. Nixon, R. A. (2013) The role of autophagy in neurodegenerative disease. *Nat. Med.* **19,** 983–997

44. Alroy, J., Pfannl, R., Ucci, A., Lefranc, G., Frattini, A., and Mégarbané, A. (2007) Electron microscopy findings in skin biopsies from patients with infantile osteopetrosis and neuronal storage disease. *Ultrastruct. Pathol.* **31,** 333–338

45. Sobacchi, C., Schulz, A., Coxon, F. P., Villa, A., and Helfrich, M. H. (2013) Osteopetrosis: genetics, treatment and new insights into osteoclast function. *Nat. Rev. Endocrinol.* **9,** 522–536